Lawrence Berkeley National Laboratory
Recent Work

Title
Reactive binder and aggregate interfacial zones in the mortar of Tomb of Caecilia Metella concrete, 1C BCE, Rome

Permalink

Journal

ISSN

Authors
Seymour, LM
Tamura, N
Jackson, MD
et al.

Publication Date

DOI

Peer reviewed

Reactive binder and aggregate interfacial zones in the mortar of Tomb of Caecilia Metella concrete, 1C BCE, Rome

Linda M. Seymour, Nobumichi Tamura, Marie Jackson*, Admir Masic*

Last updated 26 October 2021

Abstract

Integrated spectroscopic analyses and synchrotron X-ray microdiffraction investigations provide insights into the long-term reactivity of volcanic aggregate components and C-A-S-H binder of mortar samples from the robust concrete of the sepulchral corridor of the Tomb of Caecilia Metella, 1st C BCE, Rome, during the past 2050 years. The results of micrometer-scale analytical maps suggest that dissolution of Pozzolane Rosse tephra components – scoriae, clinopyroxene and leucite crystals – begins with pozzolanic reactions and the production of C-A-S-H binder but that these components remain reactive. They undergo further changes that lead to long-term remodeling of the original pozzolanic fabric of the mortar. The C-A-S-H binding phase has been reorganized into elongate features, some with a nanocrystalline preferred orientation, apparently resulting from chemical and structural destabilization through excessive incorporation of Al^{3+} and K^+ released through leucite dissolution. Resistance to failure may result from

the intermittent toughening of the interfacial zones of scoriae and clinopyroxene crystals, with post-pozzolanic mineral cements such as strätlingite and Al-tobermorite. Roman builders' selection of a leucite-rich facies of Pozzolane Rosse tephra as aggregate and the construction of the tomb in an environment with high surface and ground water exposure apparently increased beneficial hydrologic activity and reactivity in the concrete.

I. Introduction

The Tomb of Caecilia Metella is a large concrete and dimension-stone circular drum at the third milestone of the Via Appia Antica built in 30–10 BCE.[1, 2] The monument marks a pivotal transition from republican era concrete construction in Rome to the highly sophisticated concrete architecture of the imperial era (27 BCE through early fourth century CE) (Fig. 1a, b). Faced with blocks of highly durable travertine, the circular tomb rests on a square base of concrete with coarse aggregate (*caementa*) quarried from the Capo di Bove lava flow (Fig. 1b). Inside, a conical-shaped sepulchral chamber with an open oculus housed the body of Caecilia Metella, a member of the influential Caecilius Metellus family and probably the daughter-in-law of Marcus Licinius Crassus, who formed the first triumvirate in 59 BC with Julius Caesar and Pompey the Great.[3] The circular concrete structure, originally 21 m tall and 29 m in diameter, has walls 7 m thick that

2

are open to precipitation through the oculus and to ground water penetration in the lower mortuary chamber.[1, 4] Nevertheless, this structure preserves some of the most elegant and refined brick-faced concrete masonry (*opus testaceum*) of late republican Rome (Fig. 1c). The concrete of the cylindrical wall has brick coarse aggregate (*structura testacea*)[1] and remains highly cohesive despite nearly 2050 years of exposure to infiltration of rain water, ground water and high humidity within the concrete core of the monument.

The lower chamber of the tomb was excavated through deposits erupted from nearby Alban Hills volcano (Fig. 1b): the Capo di Bove lava and scoria (227±2 ka before present) and weakly-consolidated tephra of the mid-Pleistocene Pozzolanelle pyroclastic flow, (395±4 ka).[5, 6] The tephra used in the production of the highly cohesive, hydrated lime-volcanic ash mortar that binds the concrete in the lower chamber, however, was excavated from the Pozzolane Rosse pyroclastic flow (456±3 ka); the closest exposures are 0.5–0.75 km distant to the NW.[7] This voluminous eruption from Alban Hills volcano filled deep valleys eroded during marine isotope stage 12 of the deep-sea $\delta^{18}O$ record[8] with thick deposits of tephra that subsequently underwent progressive alteration. There are three principal alteration facies with different authigenic mineral assemblages: superficial horizons that interacted with surface waters producing a paleosol and greatest alteration facies, deeper horizons that interacted with ground waters, producing a least altered facies and, in the intervening deposits, an intermediate facies of alteration.[9]

3

Roman builders of the second and early first century BCE mainly employed alluvial deposits as aggregate in the mortars of concrete structures, as well as Pozzolanelle and the greatest alteration facies of Pozzolane Rosse.[10, 11] The mortar binds decicentimeter-sized rock aggregate to produce a conglomeratic concrete, described as *caementicia structura* by the Roman architect and engineer, Marcus Vitruvius Pollio, in about 30 BCE (*de architectura* 2.4.1, 2.7.5). The volcanic tephra, or excavated sands, in these mortars (*harenae rubrae, nigra* and *cana*) were described by Vitruvius (*de architectura* 2.6.1-2.6.6) and systematically correlated in republican and imperial era concrete structures by an astute Roman archaeologist, Esther Boise Van Deman.[12, 13] Van Deman described a rapid transition to more cohesive mortars in late first century BCE "by Augustus, or by his predecessor Julius Caesar" as "an epoch in the history of concrete construction."[12, 13]

Vitruvius wrote *de Architectura* for Octavian, who would become Emperor Augustus in 27 BCE; he was also a contemporary of Caecilia Metella. The concrete substructure of the Theater of Marcellus, constructed by Julius Caesar in 44 BCE, and the structure of the theater, constructed by Octavian mainly between 23–17 BCE, use the intermediate alteration facies of Pozzolane Rosse; the wall structures reveal some of the earliest *opus testaceum* masonry in Rome.[10, 14, 15] The mortars have a robust cementing matrix with calcium-aluminum-silicate-hydrate (C-A-S-H) binder; strätlingite ($Ca_2Al_2SiO_2(OH)_{10} \cdot 2.25H_2O$)[16] mineral cements are also present.[10] An recent

4

experimental reproduction of a nearly identical mortar fabricated at the Markets of Trajan about 140 years later indicates that the C-A-S-H was produced pozzolanically through the reaction of hydrated lime (Ca(OH)$_2$) with Pozzolane Rosse components but that the strätlingite formed after calcium hydroxide was fully consumed.[17] The concrete of the humid sepulchral corridor of the Tomb of Caecilia Metella[1, 4] is exceptionally compact, with highly cohesive contacts between bricks and mortar and a general absence of macrocracks in the *opus testaceum* facing (Fig. 1c). The aggregate was selected from the least altered facies of the Pozzolane Rosse pyroclastic flow, which contains crystal fragments of fresh clinopyroxene and leucite, with little or no replacement by analcime, dusky red (10R 2/2 to 5R 3/4) to dark gray (N2) scoriae (Fig. 1d–e) and surface coatings of translucent halloysite and opal and, occasionally, zeolites.[9, 18]

The central purpose of this article is to describe two mortar samples from the sepulchral corridor to gain insights into the micrometer-scale processes that have contributed to high cohesion in the concrete and how Roman builders' choice of volcanic aggregate influences these processes. The complex C-A-S-H binder of the cementing matrix are first described with synchrotron X-ray microdiffraction analyses (Fig. 2) and scanning electron microscopy (Fig. 3). Next, the complex spatial and chemical relationships of interfacial zones of Pozzolane Rosse tephra components – scoria groundmass, clinopyroxene and leucite crystals – in contact with this cementing matrix are described with correlative Raman spectroscopy,

5

scanning electron microscopy (SEM) and energy dispersive x-ray spectroscopy (EDS) (Figs. 4, 5, 6). The micrometer-scale maps record a complex evolution of cementing processes. They suggest that dissolution of tephra components begins with pozzolanic reactions and the production of C-A-S-H binder at pH > 12 but that the surfaces of the tephra components remain reactive and undergo further changes that lead to long-term modifications to the original pozzolanic fabric of the mortar.[17] Analogous processes of corrosion produce beneficial post-pozzolanic Al-tobermorite and phillipsite mineral cements in ancient Roman marine concretes.[19]

The integrated analyses investigate whether the C-A-S-H binding phase has dissolved and undergone reconfiguration over the past 2000 years; whether dissolution of highly potassic leucite crystals produces potentially beneficial post-pozzolanic changes in the cementing matrix or, by contrast, the deleterious and expansive alkali silica gels that cause macroscale cracking in Ordinary Portland Cement (OPC) concretes;[20-22] and finally, how long term changes in the interfacial zones of scoria, leucite and clinopyroxene could further long term cohesion and refinement of microcrack surfaces. The results provide a foundation for further investigations of the ancient binding phase and reactive interfaces in the Tomb of Caecilia Metella concretes. They may also inform the development of innovative, environmentally-friendly concrete infrastructure designed to replicate this long-term reactivity and to promote beneficial interactions between the hydrological environment and microstructural cementing processes.

6

II. Materials and Analytical Methods

The mortar samples were collected from the humid first century BCE concrete masonry of the Muñoz corridor in the lower structure of the Tomb of Caecilia Metella in 2006 (Fig. 1c, see also reference [1]). Figures 2, 3 describe the 06-CMETELLA-C1 sample from the brick facing of the concrete wall while Figures 4, 6, 7 describe the 06-CMETELLA-C2 sample from the crest of the barrel vault of the Muñoz corridor.

(1) Sample Preparation

Superglue™ adhesive and an embedding medium (Epo-Tek™ epoxy) were used in the preparation of the polished thin sections. Areas selected for synchrotron μXRD investigations were cut from the glass-mounted thin section with a precision saw. The 0.3-mm thick mortar slices were detached from the glass with nitromethane and mounted on adhesive tape for the beamline experiments. Raman analyses were performed on polished thin sections, since the irregular surface of the beamline specimens on tape interfered with the spectroscopic signal. Petrographic studies of polished thin sections used an Olympus BX53M microscope in the Bowen Laboratory, Department of Geology and Geophysics, University of Utah (Figs. 1, 7).

(2) X-ray microdiffraction (µXRD)

Experiments at Advanced Light Source Beamline 12.3.2 investigated submicron-sized phases with microdiffraction using a monochromatic X-ray beam (Fig. 2).[23, 24] The mortar slice mounted on tape was loaded in transmission mode, with the detector placed at 39° to the incident beam. A monochromatic X-ray beam of 10 keV was focused to 2 x 5 µm spot size. A DECTRIS Pilatus 1M area detector placed at about 150 mm recorded Debye rings from crystalline phases. The experimental geometry was calibrated using α-Al2O3 powder. X-ray diffractograms were produced with d-spacing reflections integrated radially for 2θ 4 – 54° over a 40° arch segment (χ) around the cone of diffraction. These are shown as Debye diffraction plots (Fig. 2b, c, e) and intensity versus d-spacing plots (Fig. 2d). For a high precision powder X-ray diffraction analysis of the 06-METELLA-C2 sample, see reference [18]. Data were processed using the XMAS software.[25]

(3) Raman Spectroscopy

Raman spectroscopy was performed with a WiTec Alpha 300 R confocal Raman microscope (Figs. 4–7). Samples were imaged using a Zeiss Epiplan-Neofluar 100x objective lens (NA 0.9). Samples were excited with a Research Electro-Optics 35 mW helium-neon 633nm laser at 1/3 power. Two accumulations of 45 s each were averaged at each point in the scan and a 600 g/mm spectrometer grating was used. Lateral resolution for area scans varied from 4 – 5 µm. Data were processed using the WiTec Project 5

8

software. After background removal, the signal from the embedding medium was subtracted from each scan. The software's built in k-means clustering function was used to identify component spectra of each scan. Maps indicating the intensity of each component at all points in the scan were then generated. For the peak broadening analysis of the leucite distribution, a central difference second derivative approximation was used to determine the position of the three composite peaks. These positions were used as the location for the fitted Gaussian curves in the WiTec Project 5 software. Full width at half maximum values were plotted using MATLAB R2020a.

(4) Scanning electron microscopy and energy dispersive x-ray spectroscopy

The SEM-EDS data in Figures 3c-h, 4 and 6 were acquired on a Tescan Vega 3 XMU scanning electron microscope in variable pressure mode (20 Pa, gas: N_2, accelerating voltage: 20 keV). EDS maps were acquired with a Bruker XFlash 630 silicon drift detector with sufficient acquisition time to achieve at least 2,000 counts per pixel in the mapped area to detect elements ≥1 wt%. To compare compositions of the C-A-S-H structures in Fig. 3, five point analyses were carried out on each structure type using the "exhaustive" setting (10^6 total counts per spectrum) to achieve an error ≤ 0.15 wt% in quantification of Al, Si, K and Ca. EDS data were quantified using the Bruker Esprit 2.1 Software with PB Linemarker-ZAF correction.

9

The SEM BSE images of Figures 1, 2 and 3a-b were acquired using the JOEL IT3000 at the Energy & Geoscience Institute (EGI) at the University of Utah using uncoated thin sections with an accelerating voltage of 25 kV, a beam (probe) current of 65 nA, and low vacuum at 100Pa. The primary detector used for imaging was a compositional back-scattered-electron (BSE) detector.

III. Results

The mortar of the Tomb of Caecilia Metella concrete is composed of granular particles of Pozzolane Rosse tephra that are bound together by a complex cementing matrix, consisting of a binding phase and fine sand-sized Pozzolane Rosse tephra (Fig. 1d). The coarser fraction of tephra can be considered as aggregate, yet it has the same composition as the fine ash of the cementing matrix. Both are composed of scoriae (and microscoriae <0.1 mm) with a highly potassic, silica-depleted groundmass, primary volcanic crystals of clinopyroxene, leucite, and authigenic components of analcime replacing leucite. The scoriae also contain opal and halloysite clay mineral coatings produced by long-term alteration in the pyroclastic flow deposit.[9] Petrographic micrographs demonstrate that most clinopyroxene and leucite crystal fragments, regardless of size, have dissolution and/or alteration rims around their perimeter (Fig. 1d). These could be interpreted as relics of pozzolanic processes; however, the perimeters of leucite crystals, in particular, show serrated edges that grade into the extant cementing matrix

10

suggesting dissolution that postdates the early pozzolanic reactions, which produced the C-A-S-H binder.

The components of the binding phase show three principal features: 1) discrete domains of partially intact C-A-S-H approximately 20–50 μm in size, that exhibit linear traces and splitting along these traces (Fig. 1f *site 2, see also Fig. 2a and Fig. 3a sites 2a, 2b*); 2) elongate features and incipient elongate features that, in some instances, appear to develop by splitting of the C-A-S-H domains (Fig. 3a *sites 2a, 2b*, Fig. 3b *site 1*, Fig. 3c *sites 3a, 3b*); and 3) thin, fine wispy features associated with apparent dissolution of C-A-S-H domains (Fig. 1f *site 1*; Fig. 3a *surrounding sites 2a and 2b*, 3c *above site 4*). The elongate features are more common in the 06-CMETELLA-C1 sample and the wispy features are more common in the 06-CMETELLA-C2 sample. In some instances, clinopyroxene crystals have developed alteration rinds from which incipient elongate features protrude (Fig. 1d-f *site 3*). Together, the microstructures in the C-A-S-H binding phase, the alteration rinds of clinopyroxene with incipient elongate features (Fig. 1d *site 3*) and the ragged edges of leucite crystals (Fig. 1d *site 2*) suggest pervasive processes of dissolution and reorganization in the mortar that have not been identified in previous studies of late republican and imperial era architectural concretes in Rome.[10, 17, 26, 27] The analytical descriptions of microstructures in Figures 2–7 provide insights into these diverse processes.

11

(1) Cementing Matrix µXRD, SEM-EDS

The SEM image of Figure 2a shows a typical example of the Pozzolane Rosse microscoriae and binding phase that form the cementing matrix of the mortar. The grid of µXRD analyses is overlain on the SEM image (Fig. 2a,e); it covers a microscoria, its interfacial zone and the neighboring binding phase. A Debye diffraction plot shows that clinopyroxene, magnetite, hematite are the principal crystals in the microscoria; fine-grained analcime and calcite are also present (Fig. 2b). This is a typical mineral assemblage of the least altered facies of Pozzolane Rosse, where very fine leucite crystals are replaced by analcime but larger leucite crystals (Fig. 6) remain mainly intact.[9] C-A-S-H binder occurs as partially intact domains (Fig. 2a) yet at the microscoria interface the C-A-S-H has apparently undergone pervasive *in situ* alteration (Figs. 2, 3a). Incipient elongate features are approximately 10 µm in length and C-A-S-H domains have diffuse perimeters partially surrounded by wispy features. The µXRD analysis of the incipient elongate features reveals a broad Debye diffraction ring with the highest intensity centered at approximately 5.4 Å and extending gradually to 3.6 Å and 6.5 Å (Fig. 2c, e *site #019*), indicating a nanocrystalline phase that also has a preferred orientation between -62° and 62° χ; there is no apparent 12 Å reflection.[28, 29] The broad expression of this diffraction pattern as compared to the crystalline components of the tephra (Fig. 2d) further describes the nanocrystalline nature of the incipient elongate features. The *d*-spacings of

the broad reflections correlate with 2.98–3.00 Å and 5.37–5.45 Å reflections in powdered C-A-S-H produced through laboratory syntheses[28] as well as other C-A-S-H syntheses.[30] The nanocrystalline preferred orientation indicates a structural organization in [101] direction that follows the morphology of the incipient elongate features. The integrated intensity of the broad 5 Å reflection of the C-A-S-H (Fig. 2e) indicates that the signal is strongest close the interface with the scoria, correlating to the incipient elongate features identified through SEM imaging (Fig. 2a). The partially intact C-A-S-H domains with traces of opening separation show no nanocrystalline structure or preferred orientation (sites circled in Fig. 2a,e).

SEM images show that the more intact C-A-S-H domains (Fig. 3a,c *sites 2a, 2b, 3*) occur throughout the cementing matrix while elongate features (Fig. 3a site *1*, 3b, 3c *site 4*, 3d *site 3b*) more commonly occur near volcanic tephra. Notably, the EDS data (Fig. 3d-h) reveal a slightly higher concentration of K (Fig. 3e) and Si (Figs. 3f) in the partially intact C-A-S-H structures (3.8 wt% K and 12.6 wt% Si, Fig. 3e,f *site 3*) compared to the elongate features (2.5 wt% K and 10.3 wt% Si, Fig. 3e,f *site 4*). Ca and Al concentrations (Fig. 3g,h), however, are similar (5.6 wt% Ca, 6.6 wt% Al in intact structures, 5.1 wt% Ca, 6.1 wt% Al in elongate features). These values indicate very low values for Ca/(Si+Al): 0.29 for the partially intact C-A-S-H domains and 0.31 for the elongate features, suggesting a small but non-negligible amount of potassium released to the mortar system. By contrast, the Markets of Trajan mortar reproduction at 180 days hydration has C-A-S-H

13

with Ca/(Si+Al) ≈ 0.8–0.9. The contiguous C-A-S-H domains in the ancient mortar have Ca/(Si+Al) ≈ 0.45–0.75 and Na2O+K2O ≈ 1.5 wt %. There is substantially greater incorporation of Al^{3+} and K^+ in the C-A-S-H of the Caecilia Metella mortar samples.

(2) Microscoria interface with the cementing matrix

A narrow zone of acicular features occupies the interface of a Pozzolane Rosse microscoria with the cementing matrix (Fig. 1d-f *site 1,* Fig. 4a *site 1*). This zone and the adjacent cementing matrix, including a clinopyroxene crystal (Fig. 1d-f *site 3*, Fig. 4a *site 3*) with an intact interior but a pronounced rind of dissolution and alteration along its perimeter, are investigated using correlative Raman spectroscopy and SEM-EDS imaging and analysis (Fig. 4) to gain insights into variations in chemical and mineralogical characteristics at the micrometer scale. These variations are shown by two grids of Raman analyses that are color coded to phase identifications (Fig. 4b, c). SEM-EDS analyses show corresponding variations in Na, Ca, Al, and Si (Fig. 4d–g). In the interfacial zone of the microscoria, the Raman spectrum of the acicular features correspond to spectra from tobermorite[31] and strätlingite crystals (Fig. 5). The reference spectra for strätlingite were acquired using the same acquisition parameters on known strätlingite crystals in the mortar of the Grande Aula wall concrete in the Markets of Trajan (see reference [17] for further information) and metamorphosed limestone xenoliths from Bellerberg volcano, Germany. The

14

strätlingite spectrum also occurs at the perimeter of the clinopyroxene crystal (Fig. 4b, see also Fig. 1 *site 3*).

By contrast, the neighboring binding phase is identified through Raman peaks at 661 cm^{-1} (SiO^{4-} bending) and 1002 cm^{-1} (SiO^{4-} stretching), consistent with laboratory synthesized C-A-S-H.[32] Note, however, that this spectrum is also similar to that of certain clinopyroxene crystals.[31] The Raman scan of the intact interior of the clinopyroxene that occurs in the nearby cementing matrix (Figs. 1d–f *site 2* and 4a *site 2*) reveals that the binding phase spectrum and the clinopyroxene spectrum can be distinguished by the positions of the dominate SiO^{4-} bending and stretching bands. The clinopyroxene spectrum is consistent with augite,[31] with the SiO$_4$ bending band at 667 cm^{-1} and the SiO$_4$ stretching band at 1010 cm^{-1}. Furthermore, the binding phase spectrum (Raman peaks of 661 cm^{-1} and 1002 cm^{-1}) occurs consistently at the interfacial zones of Pozzolane Rosse scoriae and microscoriae and throughout the cementing matrix (Fig. 6), further indicating that it corresponds to the C-A-S-H.

Quantified EDS elemental mapping (wt.%) of the scoria and cementing matrix (Fig. 4d-g) indicates a high calcium concentration in the clinopyroxene crystal and calcium enrichment in the binding phase and the scoria interface (Fig. 4e). The calcium content then decreases towards the interior of the scoria, with groundmass and volcanic crystals having higher Na, Al, and Si concentrations. The acicular phases in the interfacial zone maintain a relatively high concentration of aluminum (Fig. 4f) suggesting

15

that Al-tobermorite ($[Ca_4(Si_{5.5}Al_{0.5}O_{17}H_2)]Ca_{0.2} \cdot Na_{0.1} \cdot 4H_2O$)[33] rather than ideal tobermorite ($Ca_5Si_6H_2O_{18} \cdot 4H_2O$)[30, 33] occurs with strätlingite in the scoria interface. C-A-S-H binder has been previously shown to be the product of pozzolanic reaction with hydrated lime and Pozzolane Rosse tephra and, as such, calcium is expected to be elevated in interface.[17] However, the elevated Si and Al in the interfacial zone relative to that of the binding phase suggests that long term chemical interactions at the microscoria perimeter may have produced the crystalline phases.

(3) Leucite crystal interface with the cementing matrix

A leucite crystal fragment with an intact interior and complex zone of dissolution at its perimeter provides an instructive site for evaluating *in situ* changes at the crystal interface and the neighboring cementing matrix (Fig. 6). Three traverses mapped using Raman micro-spectroscopy describe this interfacial zone (Fig. 6a); the component spectra are identified in Fig. 6b. The leucite spectrum (blue) is most distinct in the intact crystal at the tips of traverses 1 and 2 (Fig. 6a).

In traverse 2, the leucite Raman signal abruptly stops at the edge of the intact crystal fragment; by contrast, in traverse 1 the leucite spectrum shows additional complexity, fading in intensity (Fig. 6a). For spectra acquired in traverse 1 (Fig. 6c), variations in the SiO^{4-} bending region of the leucite spectrum were examined by peak fitting with three Gaussian curves at 497 cm^{-1}, 510 cm^{-1} and 530 cm^{-1} (Fig. 6d). The peak fitting reveals a

16

broadening of the component peaks from the upper to lower sectors of traverse 1, most notably that corresponding to 497 cm^{-1} (Fig. 6c, d). In the intact crystal, this peak has a width (FWHM) of 16 cm^{-1} yet it broadens to up to 35 cm^{-1} in the lower interface with the cementing matrix. Such broadening indicates a more disordered configuration, consistent with progressive dissolution of the leucite perimeter. Note that original perimeter of the leucite originally extended beyond traverse 3, recorded by traces of relict microcracks in the crystal as well as gradients in the EDS maps (Fig. 6e–h sites marked "x"). The gradual decrease in potassium concentration extends from the crystal exterior through the transitional dissolution zone at the crystal perimeter to the potassium-enriched cementing matrix.

The Raman mapping along traverses 2 and 3 (Fig. 6a) describes variations in the binding phase in the cementing matrix immediately adjacent to the leucite dissolution zone. Here, the SEM images indicate pervasive dissolution halos and incipient elongate features protruding approximately 5 µm from the 10–15 µm domains of intact (and splitting) C-A-S-H. The Raman mapping at 5 µm grid spacing indicates that the intensity of the binding phase spectrum increases is especially strong next to microscoriae, detected from the hematite spectrum in the altered microscoria groundmass.

17

IV. Discussion

The integrated results of the microdiffraction and spectroscopic analyses indicate that the diverse components of Pozzolane Rosse tephra, including scoria groundmass, clinopyroxene and leucite crystal fragments as well as the binding produce diverse changes to the nature of interfacial zones and cementing matrix.

(1) C-A-S-H microstructures

C-A-S-H binder in the mortars of the late republican Theater of Marcellus and imperial era Markets of Trajan occurs as a rather uniform, contiguous phase that extends over tens of microns.[9, 10, 19, 34] There is a general absence of nanocrystalline reflections in μXRD studies of CA-S-H in the Markets of Trajan mortars. However, strätlingite crystals up to 30 μm in length are common in the interfacial zones of the ancient mortar and its reproduction at 180 days hydration.[17] In contrast, the μXRD analysis of the Caecilia Metella cementing matrix reveals a binding phase with a dominant broad reflection that is centered at approximately 5 Å d-spacing and extends to 3.6 Å and 6.5 Å (Fig. 2). Reflections at 3.0 Å and 5.4 Å have been previously identified in studies of experimental preparations of C-A-S-H,[30, 35] though the nanocrystalline Caecilia Metella C-A-S-H is further characterized by significantly broader reflections expressed from -62° to 62° chi, instead of a full range Debye diffraction ring, indicating a preferred orientation in the nanocrystalline structure of the incipient elongate features.

18

The broader reflections in µXRD analyses of the binding phase (Fig. 2c,d) overlap with several of the intense reflections (2.9 Å, 3.0 Å, 4.7 Å) identified as clinopyroxene within the microscoria (Fig. 2d). Further, the Raman spectrum identified as binding phase (Figs. 4c, 6b) is similar to that of clinopyroxene, which exhibits a chain-silicate structure. The SiO_4^- bending and stretching peaks associated with the binding phase, however, are shifted toward lower wavenumbers as described above. These data suggest that, overall, the C-A-S-H binding phase does have short range order as a layered chain silicate. However, the lower Raman shifts and broad µXRD reflections indicate that the long range order is disrupted. This is consistent with laboratory syntheses of C-(A)-S-H with higher calcium contents, which tend towards a collection of finite silica chain lengths [36, 37] and subsequently exhibit lower wavenumber Raman shifts of SiO_4^- vibrations. Interestingly, however, the calcium content of the Caecilia Metella binding phase is very low (Ca/(Si+Al) = 0.29 – 0.31), even when compared to the Markets of Trajan mortar (Ca/(Si+Al) = 0.45 – 0.75). As calcium content decreases and aluminum content increases, alkali uptake in C-(A)-S-H has been shown to increase,[35, 38] observed here as elevated potassium in intact Caecilia Metella C-A-S-H domains (Fig. 3e). It is thus possible that the potassic ions disrupt the long-range order of the binding phase, as described in alkali-rich laboratory syntheses of C-(A)-S-H.[29, 35] The spectral resolution (4 cm^{-1}) for the Raman spectroscopic data presented here is insufficient to distinguish subtle

19

differences in the spectra associated with varying potassium contents, however.

The Raman spectrum of the binding phase is also consistent with peaks observed for C-A-S-H in the mortar of the *Baianus Sinus* breakwater marine concrete (443, 670, 994 cm^{-1}) after signal from the embedding medium is removed.[19] The absence of calcite in the Raman signal (distinguishable by a strong carbonate υ_1 vibration at ~1085 cm^{-1}) in the Caecilia Metella binding phase and the paucity of calcite and vaterite in the µXRD analyses indicate that little carbonation has occurred. However, other processes that remain poorly understood have contributed to the apparent splitting and dissolution of C-A-S-H domains, the elongate features and the production of nanocrystalline structures at the 5–50 µm scale (Fig. 3), and the diffuse wispy fabrics that surround these features. Future investigations of unembedded samples will more fully characterize the fine-scale structures and properties of these features.

(2) Interfacial Al-tobermorite and Strätlingite

Raman spectroscopy (Fig. 4a-c *site 1*) indicates the presence of strätlingite and Al-tobermorite with acicular morphologies associated with the interfacial zone of a microscoria. Strätlingite also occurs in the cementing matrix near a dissolving clinopyroxene (Fig. 4b *site 3*). The Raman peaks corresponding to strätlingite do exhibit some broadening compared to strätlingite from Bellerberg volcano and the mortar of the

20

Grande Aula wall concrete (Fig. 5). This is perhaps due to the inclusion of katoite, a hydrogarnet and cementing mineral in Markets of Trajan mortars[17] with broad peaks at ~500 and ~540 cm^{-1}.[39] Experimental reproduction of the Markets of Trajan mortar showed that strätlingite began to crystallize at ≤90 days hydration, after portlandite ($Ca(OH)_2$) was fully consumed through pozzolanic reaction processes.[17] The platey crystals then begin to toughen interfacial zones along scoria perimeters and impede the macroscale propagation of microcrack segments. These microstructures, consisting mainly of interfacial strätlingite and coalesced domains of C-A-S-H binder, are pervasive in the architectural mortars of the Markets of Trajan and the Theater of Marcellus.[10, 17] Strätlingite is far less common in the 06-METELLA-C1 and 06-METELLA-C2 mortar samples of Tomb of Caecilia Metella concrete. It is confined to intermittent localities along the perimeter of occasional tephra and has not been detected in the cementing matrix. The elongate features that are ubiquitous in the cementing matrix of the 06-METELLA-C1 mortar (Fig. 3) do not show crystalline or spectroscopic indicators of strätlingite and remain an enigma worthy of further study. Still, they indicate that the original pozzolanic interfacial zone and binding phase have undergone progressive evolution at ambient temperatures, high relative humidity, and ground and surface water penetration and that this evolution has led to localized toughening of some interfacial zones..

21

(3) Leucite dissolution into cementing matrix

Progressive dissolution of the perimeter of a leucite crystal is associated with broadening of Raman bands and steep gradients in elemental compositions that persist through 25 – 100 μm of the neighboring cementing matrix (Fig. 6). A narrow potassic rind, 10 – 50 μm in thickness, with some depletion of Al and Si, occurs at the edge of the more-or-less intact crystal (Fig. 6e-h) but there is no evidence for expansive behavior or microcracks that would be associated with alkali-silica-reaction in ordinary Portland cement (OPC) concretes. There is, however, an elevated EDS spectroscopic signal for potassium in the broad leucite interfacial zone compared with the more distant cementing matrix (Fig. 6e). Where potassium concentrations are elevated (Fig. 3e *site 3*), C-A-S-H domains have halos of protruding, linear and wispy features that suggest pervasive *in situ* dissolution and reconfiguration of the pozzolanic binding phase, whereas in the more distant cementing matrix the C-A-S-H domains appear more intact. The intensity of the Raman spectra of the binding phase is strong in immediate contact with microscoria (Fig. 6a *traverse 3*) where intact C-A-S-H domains are, perhaps, more prevalent. It is possible that elevated potassium elsewhere in the dissolution zone has contributed to de-stabilization of the C-A-S-H domains and a decrease in the intensity of the Raman spectra of the binding phase.

22

4) Insights into Chemical and Mechanical Resilience

The interface between aggregates and cementing binder is of primary interest for concrete durability studies. The interfacial transition zone in OPC mortar and concrete is susceptible to a variety of degradation pathways including mechanical failure[40-42] and alkali-aggregate reaction (AAR).[43] Aggregates are selected to be inert, with very low contents of amorphous silica and alkali, $Na_2O + K_2O \leq 0.6$ wt%,[44] to reduce expansive and deleterious reactions. However, the inert aggregate consequently has a porous interfacial transition zone with the cement paste that is prone to interfacial crack propagation.[45] The addition of supplementary cementitious materials, such as silica fume, fly ash and slag, to OPC concrete has been shown to densify the interfacial transition zone by consuming the excess portlandite that disrupts the packing of cementing phases.[46-48] Such densification is expected to lower permeability and improve the mechanical performance of the concrete, thus reducing degradation effects.

Post-pozzolanic processes, or the evolution of the mortar after portlandite ($Ca(OH)_2$) has been fully consumed, have been linked to durability in both ancient Roman architectural[17] and marine[19] constructions. In the reproduction of the Markets of Trajan mortar, strätlingite crystallizes at the interface of volcanic aggregate particles only after portlandite has been fully consumed through pozzolanic reactions and production of C-A-S-H binder.[17] Further, numerous articles describe the incompatibility of

23

portlandite and strätlingite.[16, 49] Mature strätlingite fabrics have developed in the Markets of Trajan mortar[17] suggesting that crystallization could continue throughout the long term history of the concrete. In Roman marine concretes *in situ* dissolution of tephra components has also produced post-pozzolanic mineral cements, principally Al-tobermorite and phillipsite, but also strätlingite in the case of sanidine dissolution.[19]

The paucity of calcite and vaterite in intact regions of the binding phase in the Caecilia Metella mortar suggests that 1) pozzolanic reaction processes went to completion so that no portlandite remained to carbonate and 2) subsequent carbonation of the binding phase is very limited. When post-pozzolanic dissolution of silicate components of the tephra aggregate occurred alkali-rich gel formation was not favored, possibly due to insufficient calcium availability. This is in stark contrast to OPC mortars and concretes, in which portlandite is a by-product of hydration and critical to maintaining passivation of steel reinforcement. Portlandite is nearly always available to progress to AAR. It is possible that some aged blended cement concretes could approach a post-pozzolanic state, though portlandite is still detected in a fly ash and slag cement paste after 20 years hydration.[46] However, Al-tobermorite has recently crystallized in the thick OPC concrete walls of a decommissioned nuclear power plant in Japan in the absence of portlandite at 40–55°C and 16.5 years hydration, greatly increasing the strength of the concrete.[51]

24

In the two Tomb of Caecilia Metella mortar samples investigated here, post-pozzolanic crystalline mineral cements are not readily detected in the binding phase. It is apparent, however, that C-A-S-H domains (Figs. 2a, 3a *sites 2a, 2b*) have undergone substantial change to produce incipient elongate features (Figs. 2a, 3a *site 1*) and elongate features (Fig. 3b *site 1, 3c site 3b,* Fig. 3c, *site 4*)) — and that the cementing matrix has remained exceedingly robust in maintaining cohesion in the concrete during these processes. By contrast, strätlingite and Al-tobermorite mineral cements occur at the perimeter of clinopyroxene crystals and scoriae (Fig. 4, 5), suggesting intermittent toughening of the interfacial zones of these aggregate components. It may be that the reorganization of the C-A-S-H domains through excessive incorporation of aluminum and potassium released by leucite dissolution (Fig. 6) to create elongate features provides obstacles to microcrack propagation in the cementing matrix of the mortars. Further, a microcrack identified through petrographic analysis (Fig. 7a) reveals regions of infill between the crack walls (Fig. 7). The Raman spectra of four points within this region were averaged to reduce noise (Fig. 7c). Peaks corresponding to the cementing binding phase (661 cm^{-1}, 1001 cm^{-1}) are present at moderate intensity while a carbonate peak corresponding to calcite (1085 cm^{-1}, CO_3 stretching) is strong. The calcite suggests that either the mortar failed along a weaker, carbonated portion of the binder or that secondary calcite precipitated, reinforcing the crack. The presence of infill suggests the latter, and provides a starting point for future investigations

25

into the post-pozzolanic remodeling of microcracks in the mortar microstructure.

Roman builders' selection of the least altered facies of the Pozzolane Rosse pyroclastic flow, which contains abundant fresh leucite, for the mortar of the Tomb of Caecilia Metella concrete and their placement of the cylindrical structure in an environment open to saturation by ground and surface waters may be the critical factors in the development of the unusual fabrics in the binding phase and the reactive interfacial zones of the tephra components. The monumental structures designed by the contemporaries of Caecilia Metella, the Theater of Pompey and the Theater of Marcellus, mainly use the intermediate alteration facies of Pozzolane Rosse, with leucite largely replaced by analcime, in concretes within covered architectural elements, thus reducing hydrologic activity and the apparent reactivity of the binding phase. That all three structures have survived as functional monuments for 2000 years is a testament to the descriptions of another contemporary, Marcus Vitruvius Pollio, that "the test of excellence of all work can be considered in three parts: fine workmanship (*subtilitate*), magnificence (*magnificentia*), and design (*dispositione*)" (*de architectura* 5.7.5).

V. Conclusions

Mortar samples from the lower structure of the Tomb of Caecilia Metella record an exceptionally heterogeneous and complex series of reactive processes in the binding phase of the cementing matrix and the

26

interfacial zones of tephra components — scoria, clinopyroxene and leucite crystal fragments. These processes postdate early pozzolanic reaction and have contributed to substantial remodelling of the original pozzolanic fabric of the mortar. The integration of X-ray microdiffraction with spectroscopic methods provides new insights into the evolution of the cementing microstructures and provides an instructive reference for further study of concretes in ancient monuments and infrastructure that have remained intact and functional for two millennia. Resistance to failure may result from the evolution and reconfiguration of the interfacial zones of reactive aggregate components, scoriae and clinopyroxene crystals, with post-pozzolanic mineral cements such as strätlingite and Al-tobermorite. C-A-S-H binder produced through pozzolanic processes has undergone substantial reconfiguration through incorporation of alumina and potassium derived from pervasive dissolution of leucite. Roman builders' selection of a leucite-rich facies of Pozzolane Rosse tephra as aggregate and the construction of the tomb in an environment with high surface and ground water exposure, increased beneficial hydrologic activity and reactivity in the concrete.
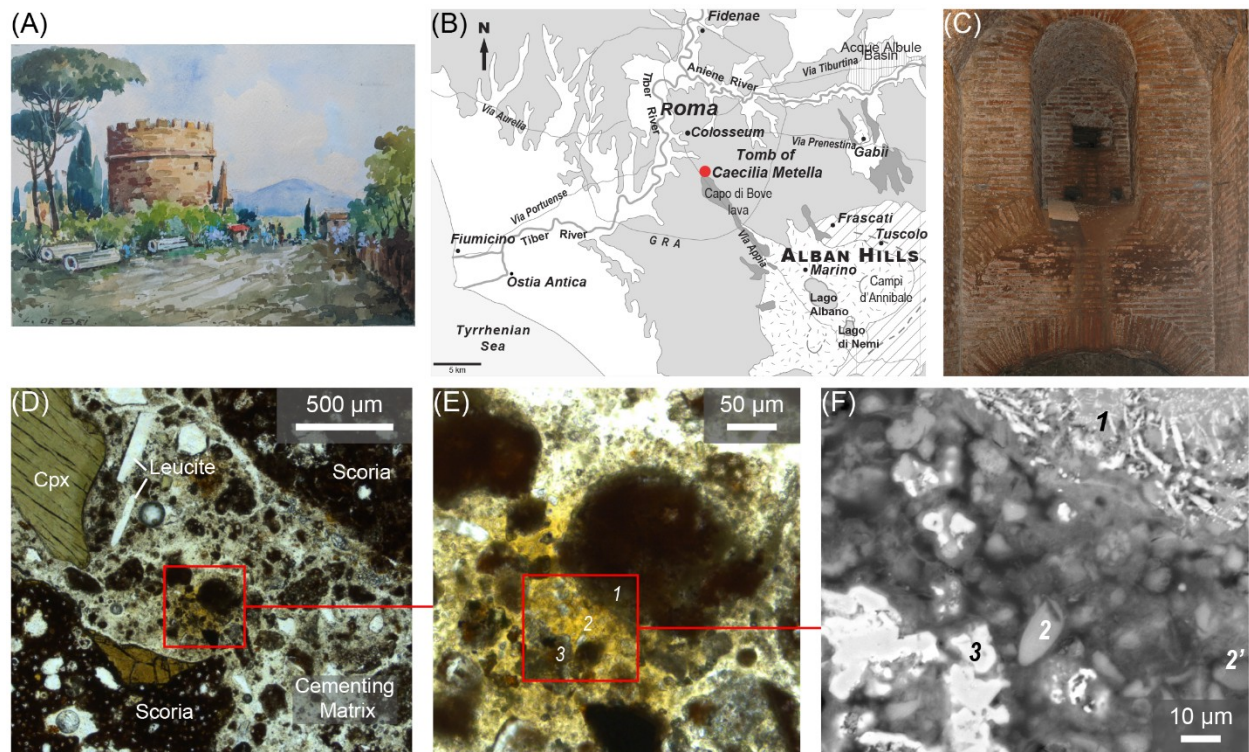
Fig. 1. The Tomb of Caecilia Metella. (a) the cylindrical structure with the Colli Albani volcano in the background (L. de Bei, courtesy of A. Masic). (b) geologic map showing location of the tomb at the tip of the Capo di Bove lava flow (after Jackson and Marra, ref. [7]). (c) *Opus testaceum* concrete of the sepulchral corridor (M. Jackson). (d, e) Pozzolane Rosse tephra components in the mortar fabrics, plane polarized light (PPL) showing the interfacial zone of a microscoria (*1*), the C-A-S-H binding phase of the cementing matrix (*2*) and the altered rind of a clinopyroxene crystal (*3*) of the 06-CMETELLA-C2 mortar sample. (f) SEM-BSE image showing these features at higher magnification: acicular features in the interfacial zone (*1*), an altered C-A-S-

H domain (*2*) and wispy features (*2'*) in the binding phase, and the diffuse

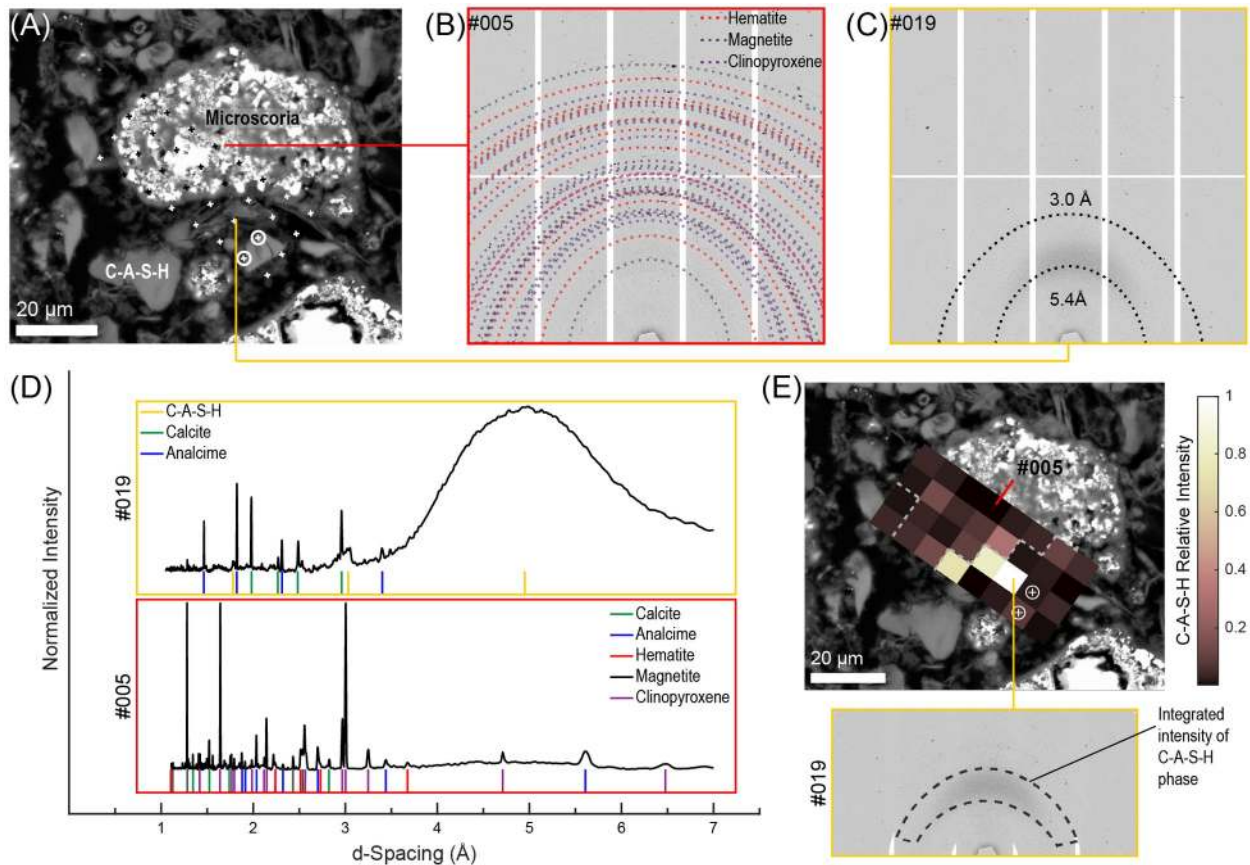border of the clinopyroxene (*3*) (see also Fig. 4).

Fig. 2. X-ray microdiffraction analyses of the cementing matrix of the 06-CMETELLA-C1 mortar sample. (a) BSE micrograph of Pozzolane Rosse microscoriae and C-A-S-H. (b) Debye diffraction plot (#005) showing clinopyroxene, magnetite and hematite crystals in the microscoria. (c) Debye diffraction plot (#019) of incipient elongate features in the binding phase with broad *d*-spacings centered at 3.0 Å and 5.4 Å. (d) intensity integrated over 2θ reveals the breadth of the C-A-S-H reflections as compared to the

29

crystalline phases in the microscoria. (e) integrated intensity over the region of C-A-S-H features (identified in lower panel) indicates the phase with nanocrystalline preferred orientation occurs predominantly in the interface of the scoria and cementing matrix at the location of the incipient elongate features. Mineral assignments from RRUFF.[31]
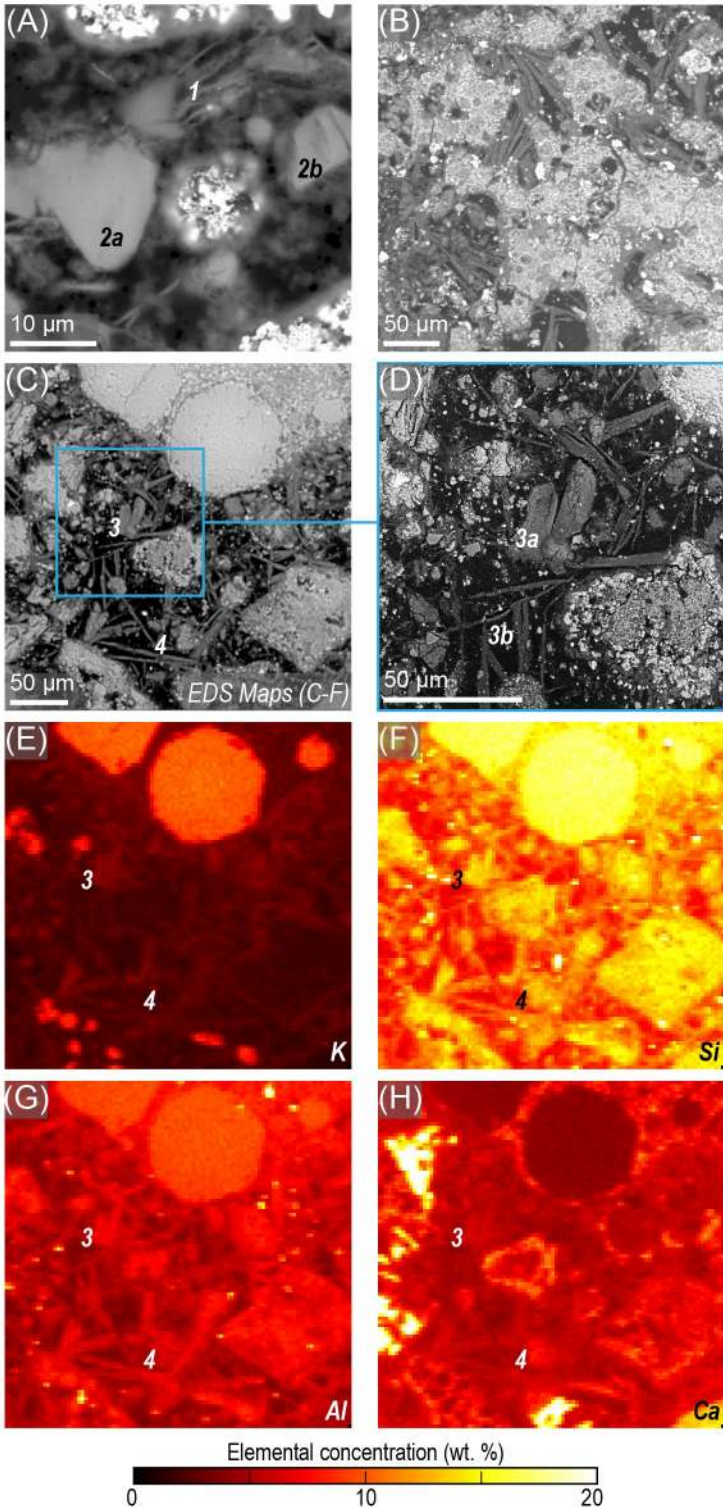
30

Fig. 3. SEM-BSE and EDS images of C-A-S-H microstructures in the 06-CMETELLA-C1 mortar sample. (a) higher magnification image of the area of

31

μXRD analyses showing incipient elongate features (*site 1*, see also Fig. 2), incipient splitting of C-A-S-H domains (*sites 2a, 2b*) and apparent dissolution and production of wispy features around C-A-S-H domains. (b) pronounced splitting of C-A-S-H domains into elongate features occurs in the interfacial zone and vesicles (*site 1*) of a large scoria. (c, d) overview of the diverse features of the binding phase showing partially intact C-A-S-H domains (*sites 3a, 3b*) and elongate features (*site 4*). (e-h) quantified EDS maps (wt %) of K, Ca, Al and Si, respectively, in the cementing matrix.
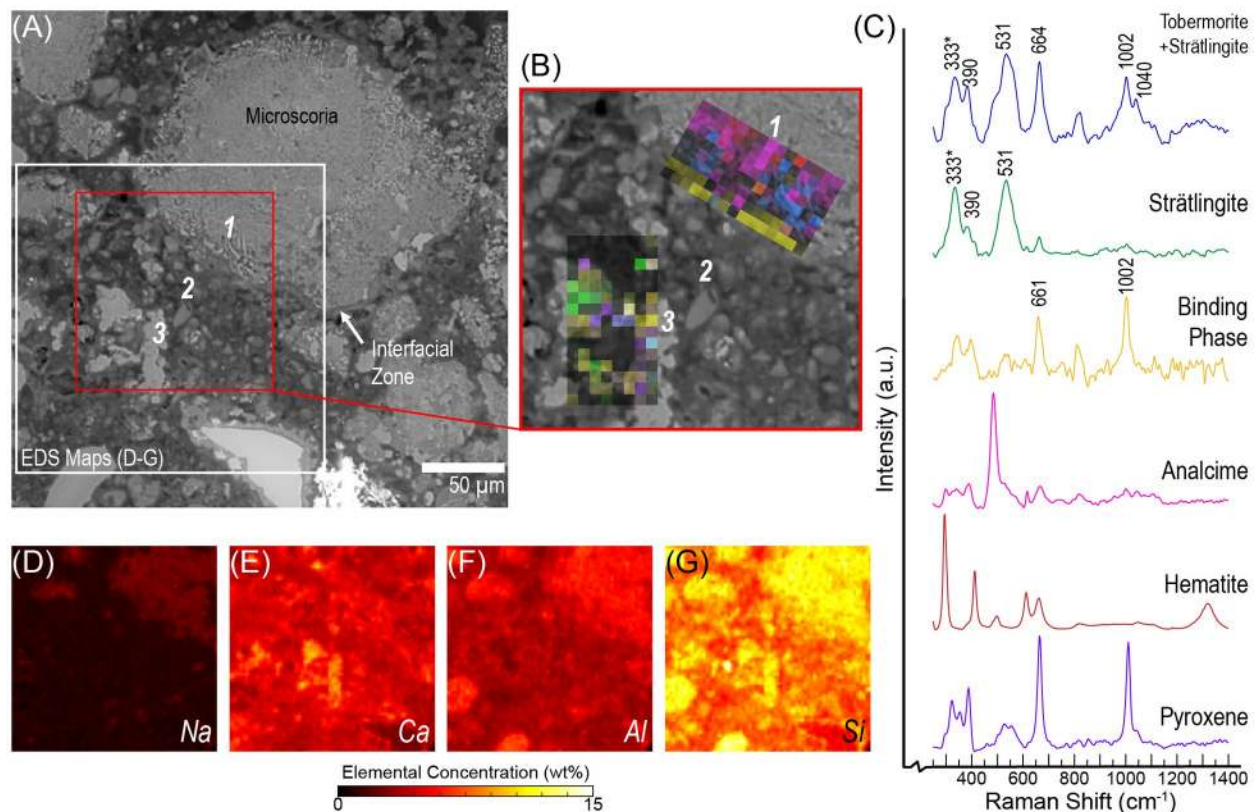
Fig. 4. Correlative Raman and SEM-EDS spectroscopic analyses describe the interface of a Pozzolane Rosse microscoria and the surrounding cementing matrix (see also Fig. 1d-f), 06-CMETELLA-C2 sample. (a) SEM-BSE micrograph shows the interfacial zone (*site 1*), the binding phase (*site 2*) and a partially altered clinopyroxene crystal (*site 3*). (b) Raman imaging (overlain on the SEM-BSE micrograph) shows the distribution of crystals in the tephra (pyroxene, hematite and analcime) and cementing phases present in the interfacial zone (the C-A-S-H binding phase, strätlingite and (Al)-tobermorite) (c) color-coded Raman spectra corresponding to the components identified in (b). (d-g) elemental distributions showing the wt % concentrations of Na, Ca,

33

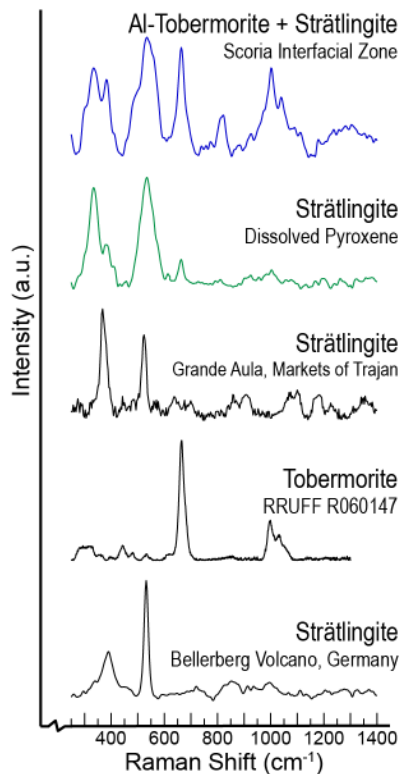Al and Si, respectively. Mineral assignments from RRUFF Project (see also Fig. 5).[31]

Fig. 5. Comparison of Al-tobermorite and strätlingite spectra from the interfacial zones of Pozzolane Rosse scoria and clinopyroxene (Fig. 4a-c) are compared to ideal tobermorite,[31] strätlingite in the wall mortar of the Grande Aula concrete, Markets of Trajan and strätlingite from Bellerberg volcanic deposits, Germany.
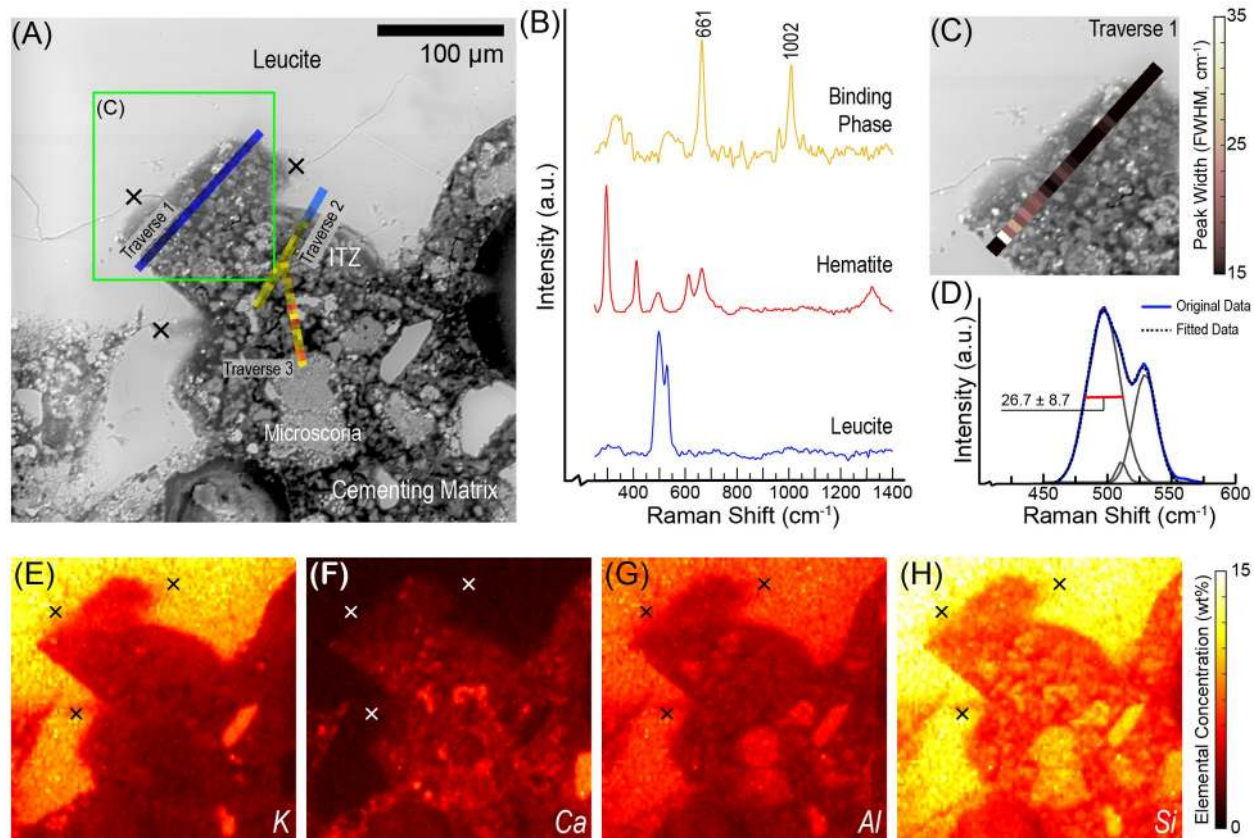
Fig. 6. Correlative Raman and SEM-EDS spectroscopic analyses reveal a gradient of dissolution in the interfacial zone of a Pozzolane Rosse leucite crystal fragment 06-CMETELLA_C2 mortar sample. (a) SEM-BSE micrograph of the leucite, interfacial zone and cementing matrix with overlays showing the distribution of phases identified via Raman imaging along traverses 1, 2, 3. The sites marked "x" indicate traces of relict microcracks in the crystal as well as compositional gradients in the EDS maps. (b) color-coded spectra of components corresponding to traverses in (a). (c) progressive dissolution of leucite in the interfacial zone is identified through a broadening of the 495 cm^{-1} SiO$_4$ bending band. (d) schematic of the full width at half maximum (FWHM) calculation plotted in traverse 1 (a, c). (e–h) Elemental distributions

35

showing the weight percent concentration of K, Ca, Al and Si, respectively. Mineral assignments from RRUFF Project.[31]
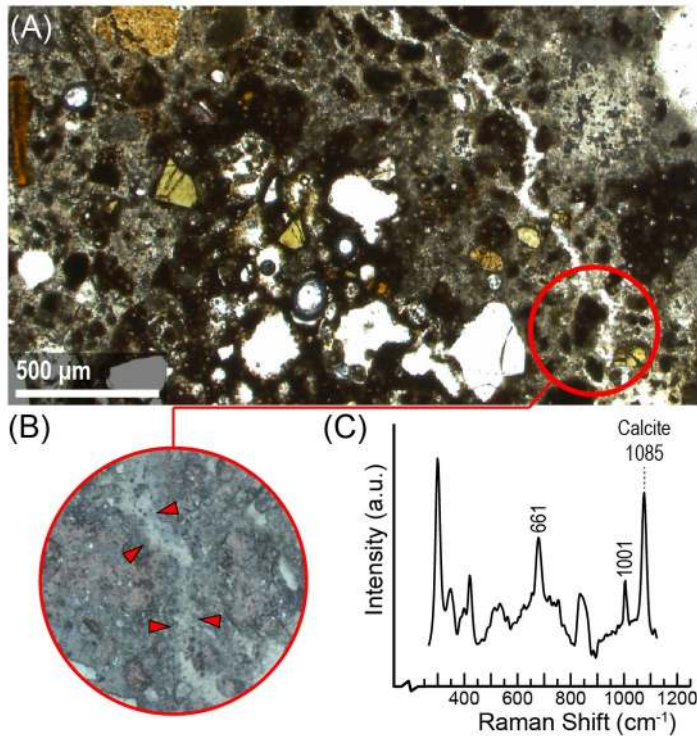

Fig. 7. Microcrack in the 06-CMETELLA-C1 mortar sample. (a) petrographic image (PPL) shows the microcrack traversing the cementing matrix, ppl. (b) reflected light confocal micrograph of an infilled area from (a) indicating the points at which Raman spectra were acquired. (c) average Raman spectrum revealing calcite as the primary component within the microcrack walls.

Acknowledgments

References

1. Gerding H. The tomb of Caecilia Metella: tumulus, tropaeum and theymele. Alnarp: Reproenheten, SLU Alnarp; 2002

2. Paris R, De Vico Fallani M, Mucci A, Marcelli M, De Filippis M, Napoletano A. VIA APPIA. *Bull della Comm Archeol Comunale di Roma*. 2000;101:333–344.

3. Coarelli F. Rome and Environs: An Archaeological Guide. 2008

4. Muñoz A. Restauri e nuove indagini su alcuni monumenti della via Appia. *BullComm*. 1913;(41):3–21.

5. Marra F, Freda C, Scarlato P, *et al.* Post-caldera activity in the Alban hills volcanic district (Italy): 40Ar/39Ar geochronology and insights into magma evolution. *Bull Volcanol*. 2003;(65):227–247.

6. Marra F, Karner DB, Freda C, Gaeta M, Renne PR. Large mafic eruptions at the Alban Hills Volcanic District (Central Italy): Chronostratigraphy, petrography and eruptive behavior. *J Volcanol Geotherm Res*. 2009;179(3–4):217–232. https://doi.org/https://doi.org/10.1016/j.jvolgeores.2008.11.009

7. Jackson M, Marra F. Roman Stone Masonry: volcanic foundations of the ancient city. *Am J Archaeol*. 2006;110(3):403–436.

8. Marra F, Florindo F, Boschi E. The history of glacial terminations from the Tiber River (Rome): Insights into glacial forcing mechanisms.

Paleooceanography. 2008;23. https://doi.org/10.1029/2007PA001543.

9.   Jackson M, Deocampo D, Marra F, Scheetz B. Mid-Pleistocene pozzolanic volcanic ash in ancient Roman concretes. *Geoarchaeology*. 2010;25(1):36–74. https://doi.org/10.1002/gea.20295

10. Jackson MD, Ciancio Rossetto P, Kosso CK, Buonfiglio M, Marra F. Building materials of the theatre of Marcellus, Rome. *Archaeometry*. 2011;53(4):728–742. https://doi.org/10.1111/j.1475-4754.2010.00570.x

11. Marra F, D'Ambrosio E, Gaeta M, Mattei M. Petrochemical Identification and Insights on Chronological Employment of the Volcanic Aggregates Used in Ancient Roman Mortars. *Archaeometry*. 2016;58(2):177–200. https://doi.org/https://doi.org/10.1111/arcm.12154

12. van Deman EB. Methods of Determining the Date of Roman Concrete Monuments. *Am J Archaeol*. 1912;16(2):230–251.

13. van Deman EB. Methods of Determining the Date of Roman Concrete Monuments (Second Paper). *Am J Archaeol*. 1912;16(3):387–432.

14. Sear F. Vitruvius and Roman theater design, American Journal of Archaeology. *Am J Archaeol*. 1990;(94):249–258.

15. Ciancio Rossetto P, Buonfiglio M. Teatro di Marcello: analisi e riflessione sugli aspetti progettuali e costruttivi. *I cantieri Edil di Roma e delle Prov Rom Stud Rom*. 2008;56(1–4):3–23.

16. Okoronkwo MU, Glasser FP. Stability of strätlingite in the CASH system. *Mater Struct Constr*. 2016;49(10):4305–4318. https://doi.org/10.1617/s11527-015-0789-x

17. Jackson MD, Landis EN, Brune PF, *et al.* Mechanical resilience and cementitious processes in Imperial Roman architectural mortar. *Proc Natl Acad Sci U S A*. 2014;111(52):18484–9. https://doi.org/10.1073/pnas.1417456111

18. Jackson M, Marra F, Deocampo D, Vella A, Kosso C, Hay R. Geological observations of excavated sand (harenae fossiciae) used as fine aggregate in ancient Roman pozzolanic mortars. *J Rom Archaeol*. 2007; (20):25–51.

19. Jackson MD, Mulcahy SR, Chen H, *et al.* Phillipsite and Al-tobermorite mineral cements produced through low-temperature water-rock reactions in Roman marine concrete. *Am Mineral*. 2017;102(7).

20. Rivard P, Ollivier JP, Ballivy G. Characterization of the ASR rim: Application to the Potsdam sandstone. *Cem Concr Res*. 2002;32(8):1259–1267. https://doi.org/10.1016/S0008-8846(02)00765-2

21. Chappex T, Scrivener KL. The effect of aluminum in solution on the dissolution of amorphous silica and its relation to cementitious systems. *J Am Ceram Soc*. 2013;96(2):592–597. https://doi.org/10.1111/jace.12098

22. Balachandran C, Muñoz JF, Arnold T. Characterization of alkali silica reaction gels using Raman spectroscopy. *Cem Concr Res*. 2017;92:66–74. https://doi.org/10.1016/j.cemconres.2016.11.018

23. Tamura N, Kunz M, Chen K, Celestre RS, MacDowell AA, Warwick T. A

superbend X-ray microdiffraction beamline at the Advanced Light Source. *Mater Sci Eng A*. 2009;(524):1–2.

24. Stan C V., Tamura N. Synchrotron X-ray microdiffraction and fluorescence imaging of mineral and rock samples. Journal of Visualized Experiments. *J Vis Exp*. 2018;(136). https://doi.org/https://doi.org/10.3791/57874

25. Tamura N. XMAS: A versatile tool for analyzing synchrotron microdiffraction data. Vol. 4. In: Ice G, Barabash B, eds. *Strain dislocation gradients from Diffr.*, Vol. 4. Singapore: World Scientific; 2014:125–155.

    https://doi.org/https://doi.org/10.1142/9781908979636_0004

26. Belfiore CM, Fichera G V, La Russa MF, *et al.* A Multidisciplinary Approach for the Archaeometric Study of Pozzolanic Aggregate in Roman Mortars: The Case of Villa dei Quintili (Rome, Italy). *Archaeometry*. 2015;57(2):269–296.

    https://doi.org/https://doi.org/10.1111/arcm.12085

27. Columbu S, Lisci C, Sitzia F, *et al.* Mineralogical, petrographic and physical-mechanical study of Roman construction materials from the Maritime Theatre of Hadrian's Villa (Rome, Italy). *Measurement*. 2018;127:264–276.

    https://doi.org/https://doi.org/10.1016/j.measurement.2018.05.103

28. Myers RJ, L'Hôpital E, Provis JL, Lothenbach B. Effect of temperature and aluminium on calcium (alumino)silicate hydrate chemistry under

40

equilibrium conditions. *Cem Concr Res*. 2015;68:83–93. https://doi.org/10.1016/j.cemconres.2014.10.015

29. L'Hôpital E, Lothenbach B, Le Saout G, Kulik D, Scrivener K. Incorporation of aluminium in calcium-silicate-hydrates. *Cem Concr Res*. 2015;75:91–103. https://doi.org/10.1016/j.cemconres.2015.04.007

30. Sun GK, Young JF, Kirkpatrick RJ. The role of Al in C-S-H: NMR, XRD, and compositional results for precipitated samples. *Cem Concr Res*. 2006;36(1):18–29. https://doi.org/10.1016/j.cemconres.2005.03.002

31. Lafuente B, Downs RT, Yang H, Stone N. The power of databases: the RRUFF project. In: Armbruster T, Danisi RM, eds. *Highlights Mineral. Crystallogr.* Berlin: W. De Gruyter; 2015:1–30.

32. Ortaboy S, Li J, Geng G, *et al.* Effects of CO2 and temperature on the structure and chemistry of C-(A-)S-H investigated by Raman spectroscopy. *RSC Adv*. 2017;7(77):48925–48933. https://doi.org/10.1039/c7ra07266j

33. Taylor HFW. Tobermorite, jennite, and cement gel. *Zeitschrift für Krist*. 1992;(202):41–50.

34. Jackson MD, Chae SR, Mulcahy SR, *et al.* Unlocking the secrets of Al-tobermorite in Roman seawater concrete. *Am Mineral*. 2013;98(10):1669–1687. https://doi.org/10.2138/am.2013.4484

35. Myers RJ, L'Hôpital E, Provis JL, Lothenbach B. Composition-solubility-structure relationships in calcium (alkali) aluminosilicate hydrate (C-(N,K-)A-S-H). *Dalt Trans*. 2015;44(30):13530–13544.

https://doi.org/10.1039/c5dt01124h

36. Abdolhosseini Qomi MJ, Ulm FJ, Pellenq RJM. Evidence on the dual nature of aluminum in the calcium-silicate-hydrates based on atomistic simulations. *J Am Ceram Soc*. 2012;95(3):1128–1137. https://doi.org/10.1111/j.1551-2916.2011.05058.x

37. Pellenq RJ-M, Kushima A, Shahsavari R, *et al.* A realistic molecular model of cement hydrates. *Proc Natl Acad Sci U S A*. 2009;106(38):16102–7. https://doi.org/10.1073/pnas.0902180106

38. Hong S-Y, Glasser FP. Alkali sorption by C-S-H and C-A-S-H gels: Part II. Role of alumina. *Cem Concr Res*. 2002;32(7):1101–1111. https://doi.org/ https://doi.org/10.1016/S0008-8846(02)00753-6

39. Black L. Raman spectroscopy of cementitious materials. *Spectrosc Prop Inorg Organomet Compd*. 2009;72–127. https://doi.org/10.1039/b715000h

40. Königsberger M, Pichler B, Hellmich C. Micromechanics of ITZ-aggregate interaction in concrete part I: Stress concentration. *J Am Ceram Soc*. 2014;97(2):535–542. https://doi.org/10.1111/jace.12591

41. Königsberger M, Pichler B, Hellmich C. Micromechanics of ITZ-Aggregate Interaction in Concrete Part II: Strength Upscaling. *J Am Ceram Soc*. 2014;97(2):543–551. https://doi.org/10.1111/jace.12606

42. Prokopski G, Halbiniak J. Interfacial transition zone in cementitious materials. *Cem Concr Res*. 2000;30(4):579–583. https://doi.org/10.1016/S0008-8846(00)00210-6

42

43. Ponce JM, Batic OR. Different manifestations of the alkali-silica reaction in concrete according to the reaction kinetics of the reactive aggregate. *Cem Concr Res*. 2006;36(6):1148–1156. https://doi.org/10.1016/j.cemconres.2005.12.022

44. ASTM International. ASTM C1260 - 14 Standard Test Method for Potential Alkali Reactivity of Aggregates (Mortar-Bar Method). 2014.

45. Landis EN, Zhang T, Nagy EN, Nagy G, Franklin WR. Cracking, damage and fracture in four dimensions. *Mater Struct*. 2007;40(4):357–364. https://doi.org/10.1617/s11527-006-9145-5

46. Kuroda M, Watanabe T, Terashi N. Increase of bond strength at interfacial transition zone by the use of fly ash. *Cem Concr Res*. 2000;30(2):253–258. https://doi.org/10.1016/S0008-8846(99)00241-0

47. Duan P, Shui Z, Chen W, Shen C. Effects of metakaolin, silica fume and slag on pore structure, interfacial transition zone and compressive strength of concrete. *Constr Build Mater*. 2013;44:1–6. https://doi.org/10.1016/j.conbuildmat.2013.02.075

48. Gao JM, Qian CX, Liu HF, Wang B, Li L. ITZ microstructure of concrete containing GGBS. *Cem Concr Res*. 2005;35(7):1299–1304. https://doi.org/10.1016/j.cemconres.2004.06.042

49. Snellings R, Mertens G, Elsen J. Supplementary Cementitious Materials. *Rev Mineral Geochemistry*. 2012;74(1):211–278. https://doi.org/10.2138/rmg.2012.74.6

50. Luke K, Lachowski E. Internal composition of 20-year-old fly ash and

slag-blended ordinary portland cement pastes. *J Am Ceram Soc*. 2008;91(12):4084–4092. https://doi.org/10.1111/j.1551-2916.2008.02783.x

51. Maruyama I, Rymeš J, Aili A, *et al.* Long-term use of modern Portland cement concrete: The impact of Al-tobermorite formation. *Mater Des*. 2021;198:109297.

https://doi.org/https://doi.org/10.1016/j.matdes.2020.109297